Performance Analysis of Forced Commutated Controlled Series Capacitor Rectifier for More Electric Aircraft

Tahani H. M. Al-Mhana , *Member, IEEE*, Volker Pickert , *Member, IEEE*, Bashar Zahawi , *Senior Member, IEEE*, and David J. Atkinson

Abstract—The forced commutated controlled series capacitor (FCSC) rectifier has been recently proposed to power stand-alone variable-voltage variable-frequency generation systems, such as the full authority digital electronic control (FADEC) system, in more electric aircraft. The employment of this rectifier helps to meet increasing power demand requirements while maintaining low current harmonic levels without the need for bulky filters. The FCSC rectifier is controlled to maintain resonance with line frequency variation by inserting variable capacitive reactance in series with the variable-frequency generator's inductive reactance. Unity power factor operation with nearly pure sinusoidal converter input currents is thus achieved, for better utilization of the generator. The FCSC rectifier operation with a variable dc on-board load is analyzed in this paper, including a description of the principle modes of operation of the circuit. The enhancement in circuit's output voltage and output power achieved by replacing the conventional diode bridge rectifier with the FCSC rectifier is also demonstrated. Both rectifiers are analyzed numerically using Saber/Synopsys over a wide range of operating voltages and frequencies. Results are experimentally verified using 1-kW laboratory test rig.

Index Terms—AC–DC power converters, forced commutated controlled series capacitor (FCSC), more electric aircraft (MEA), power factor correction (PFC).

I. INTRODUCTION

THE power levels required on board an aircraft and the complexity of aircraft electrical loads have increased substantially with the advent of the more electric aircraft (MEA). This has led to an increase in the use of power electronic circuits and devices to enhance on-board power density, efficiency and reliability, and to fulfill the requirements of power quality standards while reducing weight, volume, and the environmental footprint of the aircraft [1]–[4]. In recent years, the aircraft industry has been moving toward the use of variable-frequency, variable-voltage power supply systems to improve efficiency and reduce aircraft's volume and weight [5], [6]. In addition, significant advantages can be achieved when moving toward higher voltage on-board ac and dc power systems. These include an increase in the effective capacity and a reduction in current, which significantly reduces cable weight, mass, and circuit power losses. For example, a hybrid power system architecture of 230 V/360–800 Hz ac and ±270 V dc are used in the most advanced MEA such as Boeing 787 and Airbus A380 [7]–[10].

To supply the on-board dc load and maintain MEA power quality requirements, while coping with the main bus variable frequency (360–800 Hz), different power factor correction (PFC) ac–dc converters have been employed. These can be grouped into five main categories: active PFCs, buck, boost, buck–boost, and multilevel converters [11]–[16]. A power filter is normally employed in these circuits to comply with the strict regulations of current total harmonic distortion specified by DO-160 [17].

To avoid the use of a filter and for better utilization of the generator, a new PFC rectifier has recently been proposed [18] to replace the conventional diode bridge rectifier normally used to energize a dc load supplied by a variable-frequency, variable-voltage permanent magnet (PM) generator in MEA. An example of one such load is the full authority digital electronic control system (FADEC). The new circuit, named as forced commutated controlled series capacitor (FCSC) rectifier, is essentially a series compensation circuit characterized by its ability to improve the overall power factor to almost unity while maintaining low current harmonic distortion levels with no filter requirement over a wide range of operating voltages and frequencies, fulfilling the requirements of DO-160G [17]. In this paper, the steady-state behavior of the FCSC-rectifier circuit is analyzed analytically including a description of the principle modes of operation of the circuit. Circuit steady-state waveforms and operating characteristics are compared with those of a conventional diode bridge rectifier at different operating voltages/frequencies and at
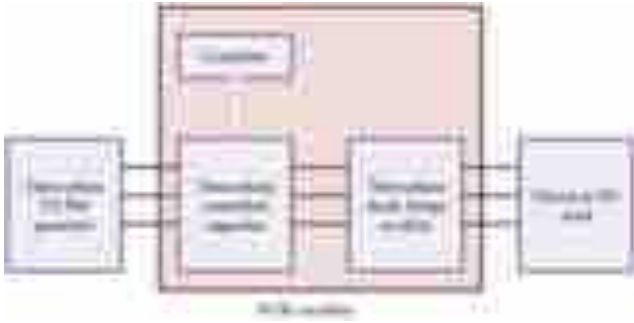
Fig. 1. FCSC-rectifier feeding dc on-board load from a variable-frequency PM generator in an MEA.
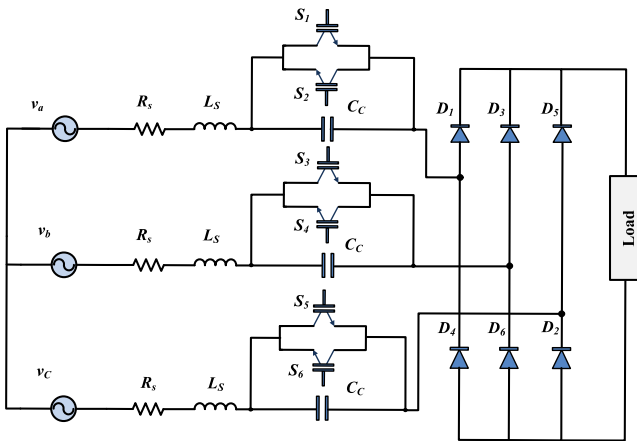

Fig. 2. Schematic diagram of the FCSC rectifier with a dc on-board load.

different load levels. Simulation results are experimentally verified over a wide range of operating voltages and frequencies using a 1-kW test bench, showing significant improvements in system performance when compared with the conventional diode bridge rectifier operation.

The remainder of the paper is structured as follows. Section II gives a brief description of the FCSC-rectifier circuit topology and its control strategy. An analysis of the FCSC-rectifier modes of operation is presented in Section III together with a description of the current commutation process. FCSC-rectifier simulation results are presented in Section IV and compared with the waveforms obtained when using a conventional diode bridge rectifier. Section V presents an experimental verification of FCSC-rectifier operating characteristics. Conclusions are presented in Section VI.

II. FCSC-RECTIFIER CIRCUIT AND CONTROL

Fig. 1 shows a block diagram of the three-phase FCSC-rectifier circuit. A forced-commutated, series compensation capacitor is inserted between the variable-voltage, variable-frequency generator and the diode bridge rectifier and controlled to maintain resonance as the frequency of the supply is varied [18]. A schematic diagram of the FCSC-rectifier circuit is shown in Fig. 2. As the frequency of the supply is varied, the duty cycles of the insulated gate bipolar transistor (IGBT) switches

are controlled to vary the injected series capacitive reactance and match the generator inductive reactance. As a result, the circuit impedance is minimized and a near sinusoidal ac current waveform is injected into the rectifier at near unity power factor. The IGBTs switching frequency is relatively low at half the frequency of the generator voltage, which helps in limiting the circuit switching losses.

The value of the compensation capacitor C_C is chosen so that resonance occurs at the maximum operating frequency of the circuit. When operating at a lower frequency, resonance is maintained by controlling the duty ratio D of the IGBT switched to reduce the effective capacitive reactance injected into the line and match the reduced value of generator inductive reactance. As the frequency of the generator voltage varies, D is increased according to the relationship

$$D = \frac{1}{2}\left(1 - \frac{f_s}{f_{\max}}\right)$$

where f_s is the operating frequency and $f_{\max}$ is the maximum frequency of the circuit. The switch conduction angle δ is the given by

$$\delta = \pi\left(1 - \frac{f_s}{f_{\max}}\right).$$

Initially, all IGBT switches are OFF, all circuit currents are zero, and the diode conduction state is determined by the relative magnitudes of generator voltages. However, once the FCSC circuit is in operation, it is important to note that the diode current commutation process in the FCSC-rectifier circuit is different from that in a conventional diode bridge rectifier. Fig. 3 shows the timing diagram of all the diodes and IGBT switches of the FCSC-rectifier circuit. Unlike a conventional rectifier circuit in which the current commutates from one conducting leg to the neighboring leg (say from D_5 to D_1 in the upper rail) resulting in the familiar six-pulse dc voltage waveform, the current in the FCSC rectifier commutates between the two diodes in the same leg (say from D_5 to D_2) resulting in a six-pulse dc current waveform. In other words, the diode conduction periods in the FCSC rectifier are determined by the direction of injected currents (the upper diodes conduct when the corresponding line current is positive and the lower diodes conduct when the current is negative). As a result, the FCSC rectifier always operates in the continuous current mode, unlike the conventional three-phase diode bridge rectifier that can operate in discontinuous mode, resulting in distorted input current waveforms. In addition, the FCSC rectifier can cope with a wide range of PM generator frequency/voltage variations because it does not suffer from the limitations imposed on conventional diode rectifier circuits by the current overlap process (especially with high values of generator inductance and at higher operating frequencies or low voltages).

III. FCSC-RECTIFIER MODES OF OPERATION

The FCSC-rectifier circuit has six modes of operation in every supply cycle, each lasting for 60°. Taking the supply phase voltage v_a as a reference, Mode 1 starts at $\omega t = 0$ and the period
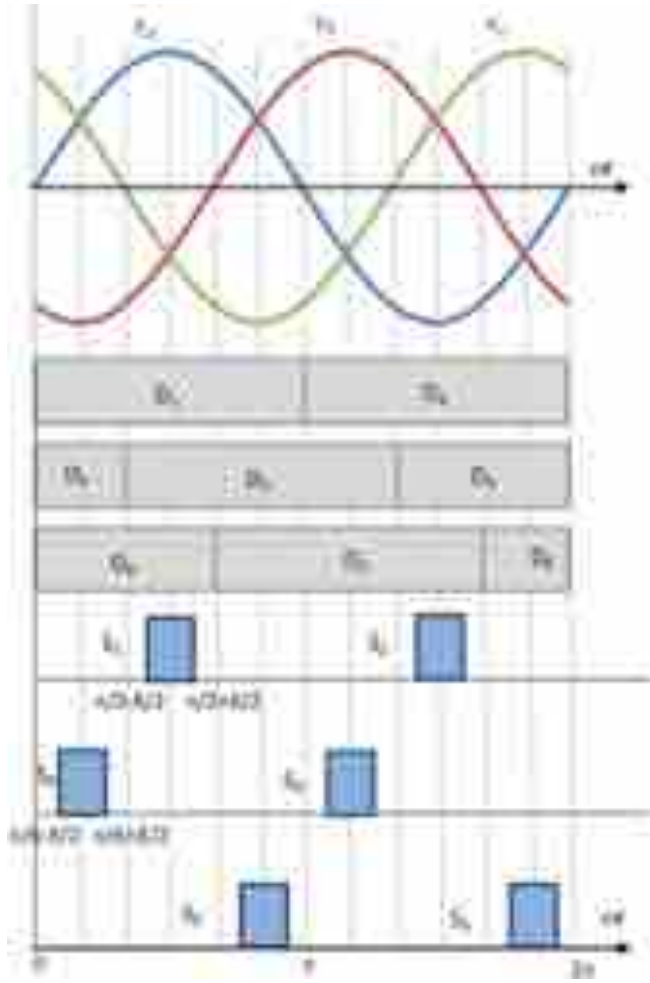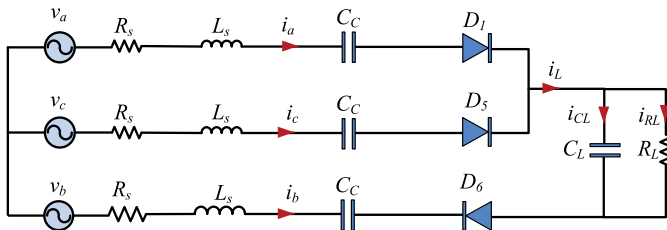
Fig. 3. FCSC-rectifier circuit timing diagram.

Fig. 4. Effective circuit during Mode 1-POA with an *RC* load.

$0 < \omega t < \pi/3$ can be divided into three distinct subperiods described here as principle operations A, B, and C. These principle operation periods are repeated every 60° (every mode) and are discussed in more detail as follows.

A. Mode 1, Principal Operation A (POA): $0 < \omega t < \pi/6 - \delta/2$: D_1, D_5, and D_6 Conduct

During this period, no IGBT switch is ON and three diodes are conducting (D_1, D_5, and D_6). The subperiod ends at $\omega t = \pi/6 - \delta/2$ when the IGBT switch S_4 is turned ON (where δ is the conduction period of the IGBT switches). During this mode of operation, $i_L = i_a + i_c = -i_b$.

Fig. 4 shows the effective circuit topology for this subperiod when feeding a parallel *RC* load.

Applying Kirchhoff's voltage law

$$L_s \frac{d^2 i_a}{dt^2} - L_s \frac{d^2 i_c}{dt^2} + R_s \frac{di_a}{dt} - R_s \frac{di_c}{dt}$$
$$+ \frac{i_a}{C_c} - \frac{i_c}{C_c} = \frac{dv_{\mathrm{ac}}}{dt}$$

$$2L_s \frac{d^2 i_a}{dt^2} + L_s \frac{d^2 i_c}{dt^2} + 2R_s \frac{di_a}{dt} + R_s \frac{di_c}{dt}$$
$$+ R_L \frac{di_{\mathrm{RL}}}{dt} + \frac{2\, i_a}{C_c} + \frac{i_c}{C_c} = \frac{dv_{ab}}{dt}$$

$$R_L \frac{di_{RL}}{dt} - \frac{i_{CL}}{C_L} = 0$$

$$i_a + i_c - i_{RL} - i_{CL} = 0.$$

Or, in a matrix form

$$
\begin{bmatrix}
L_s & -L_s & 0 & 0 \\
2L_s & L_s & 0 & 0 \\
0 & 0 & 0 & 0 \\
0 & 0 & 0 & 0
\end{bmatrix}
\begin{bmatrix}
\ddot{i}_a \\
\ddot{i}_c \\
\ddot{i}_{RL} \\
\ddot{i}_{CL}
\end{bmatrix}
$$
$$
+
\begin{bmatrix}
R & -R & 0 & 0 \\
2R & R & R_L & 0 \\
0 & 0 & R_L & 0 \\
0 & 0 & 0 & 0
\end{bmatrix}
\begin{bmatrix}
\ddot{i}_a \\
\ddot{i}_c \\
\ddot{i}_{RL} \\
\ddot{i}_{CL}
\end{bmatrix}
$$
$$
+
\begin{bmatrix}
(1/C_c) & -(1/C_c) & 0 & 0 \\
(2/C_c) & (1/C_c) & 0 & 0 \\
0 & 0 & 0 & -(1/C_L) \\
1 & 1 & -1 & -1
\end{bmatrix}
$$
$$
\begin{bmatrix}
i_a \\
i_c \\
i_{RL} \\
i_{CL}
\end{bmatrix}
=
\begin{bmatrix}
\dot{v} \\
\dot{v}_{ab} \\
0 \\
0
\end{bmatrix}
\tag{1}
$$

where v_{ab} and v_{ac} are the line–line voltages, i_a and i_c are the ac line current, R_s and R_L are PM generator internal resistance and load resistor, respectively, L_s is the PM generator internal inductance, C_C is the series compensation capacitance, and C_L is the load capacitance.

B. Mode 1, Principal Operation B (POB): $\pi/6 - \delta/2 < \omega t < \pi/6 + \delta/2$: S_4 ON, D_1, D_5, and D_6 Conduct

The transition between POA and POB occurs at $\omega t = \pi/6 - \delta/2$ when the IGBT switch S_4 is turned ON (bypassing the series compensation capacitor), and all other IGBTs are OFF while S_4 is turned OFF at $\omega t = \pi/6 + \delta/2$.
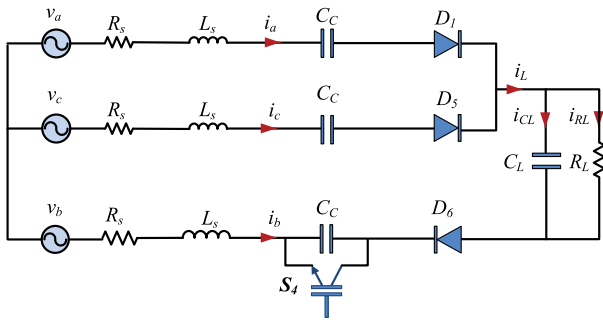
Fig. 5.   Effective circuit during Mode 1-POB with a parallel *RC* load.

Fig. 5 shows the effective circuit configuration during this subperiod when current is supplying to a parallel *RC* load.

Applying Kirchhoff's voltage law

$$L_s \frac{d^2 i_a}{dt^2} - L_s \frac{d^2 i_c}{dt^2} + R_s \frac{di_a}{dt} - R_s \frac{di_c}{dt} + \frac{i_a}{C_c} - \frac{i_c}{C_c} = \frac{dv_{ac}}{dt}$$

$$2L_s \frac{d^2 i_a}{dt^2} + L_s \frac{d^2 i_c}{dt^2} + 2R_s \frac{di_a}{dt} + R_s \frac{di_c}{dt}$$
$$+ R_L \frac{di_{\mathrm{RL}}}{dt} + \frac{i_a}{C_c} = \frac{dv_{ab}}{dt}$$

$$R_L \frac{di_{RL}}{dt} - \frac{i_{CL}}{C_L} = 0$$

$$i_a + i_c - i_{RL} - i_{CL} = 0.$$

Or, in a matrix form

$$\begin{bmatrix} L_s & -L_s & 0 & 0 \\ 2L_s & L_s & 0 & 0 \\ 0 & 0 & 0 & 0 \\ 0 & 0 & 0 & 0 \end{bmatrix} \begin{bmatrix} \ddot{i}_a \\ \ddot{i}_c \\ \ddot{\iota}_{RL} \\ \ddot{\iota}_{RL} \end{bmatrix}$$

$$+ \begin{bmatrix} R & -R & 0 & 0 \\ 2R & R & R_L & 0 \\ 0 & 0 & R_L & 0 \\ 0 & 0 & 0 & 0 \end{bmatrix} \begin{bmatrix} \ddot{i}_a \\ \ddot{i}_c \\ \ddot{\iota}_{RL} \\ \ddot{\iota}_{RL} \end{bmatrix}$$

$$+ \begin{bmatrix} (1/C_c) & -(1/C_c) & 0 & 0 \\ (1/C_c) & 0 & 0 & 0 \\ 0 & 0 & 0 & -(1/C_L) \\ 1 & 1 & -1 & -1 \end{bmatrix}$$

$$\begin{bmatrix} i_a \\ i_c \\ i_{RL} \\ i_{CL} \end{bmatrix} = \begin{bmatrix} \dot{v}_{\mathrm{ac}} \\ \dot{v}_{ab} \\ 0 \\ 0 \end{bmatrix}. \qquad (2)$$

C. Mode 1, Principal Operation C (POC): $\pi/6 + \delta/2 < \omega t < \pi/3$: D_1, D_2, and D_6 Conduct

Transition to POC occurs at $\omega t = \pi/6 + \delta/2$ when S_4 is turned OFF. All IGBT switches are OFF and circuit configuration and operation during this subperiod is identical to that during
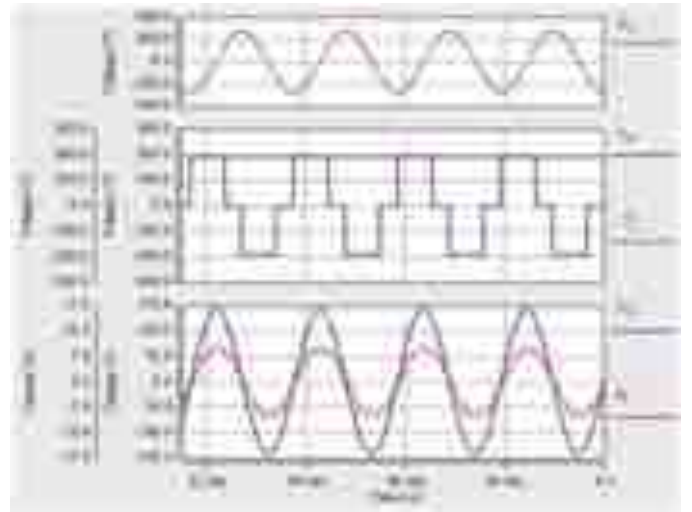

Fig. 6.   Simulated FCSC-rectifier waveforms at 480 Hz/100 V. v_{cc} is the voltage across the capacitor, v_{in} is the line-to-line voltage at the rectifier (diode bridge) terminals, v_L is the load voltage, i_S is the supply current, and v_s is the supply phase voltage.

POA. Corresponding circuit equations for operation with a re-sistive (*R*) load and an inductive load (*RL* load) are given in the appendix.

Mode 2 start at $\omega t = \pi/3$ when i_c changes polarity and the current in diode D_5 is commutated to D_2. During this mode, $i_L = i_a = -i_b - i_c$. Circuit equations for Mode 2 (and all other modes of operation) can be derived in a similar manner to those shown above for Mode 1. The above equations can be incor-porated in a computer program and solved to obtain all circuit currents and voltages, power flows, etc., (solving a new initial value problem at each circuit transition).

IV. Simulation Results

The FCSC-rectifier circuit is simulated, and its waveforms and operating characteristics are compared with those of the conventional diode bridge rectifier in this section. Simulations were carried out for a parallel *RC* load using Saber/Synopsys. To allow for direct verification of the results, simulations were conducted for voltages in the range 75–100 V over a 240 Hz frequency range from 240 to 480 Hz, in line with the mini-mum/maximum output voltage/frequency of the programmable power source used in the test bench.

All the IGBT switches are switched OFF at the maximum voltage/frequency operating point of 100 V/480 Hz. As the fre-quency of the supply drops below 480 Hz, the IGBT switches are controlled to obtain the appropriate conduction period δ and maintain series resonance. Circuit parameters are as follows: R_s and R_L are of 2.5 and 30 Ω, respectively. C_C and C_L are of 8 and 500 μF and L_s is of 13.75 mH. Fig. 6 illustrates the circuit voltage and current waveforms when the system is oper-ated at maximum voltage and frequency of 100 V and 480 Hz. Interestingly, the rectifier input ac voltage v_{in} is a square pulse varying between the positive value of load voltage ($+v_L$), zero, and ($-v_L$). Most importantly, however, the near sinusoidal ac
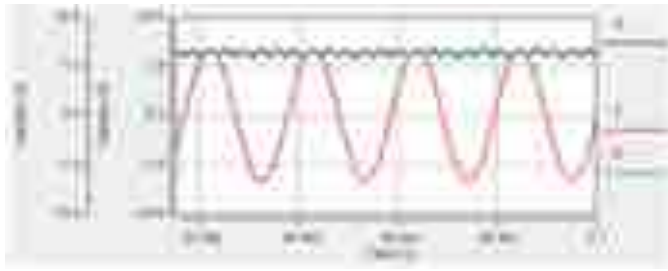
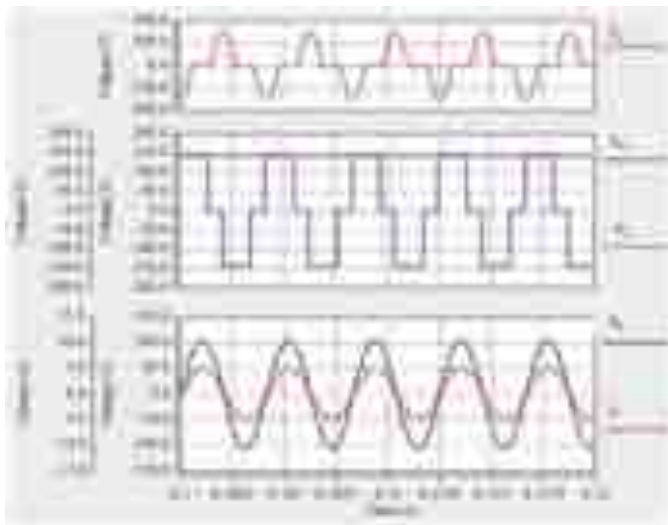Fig. 7. Simulated FCSC-rectifier dc current and the input ac current waveforms at 480 Hz/100 V.

Fig. 8. Simulated FCSC-rectifier waveforms at 240 Hz/75 V.

Fig. 9. Voltage and current waveforms for the conventional diode bridge rectifier with an *RC* load operating at 480 Hz/100 V.

Fig. 10. Voltage and current waveforms for the conventional diode bridge rectifier with an *RC* load operating at 240 Hz/75 V.

line current is maintained in-phase with the generator ac voltage waveform, giving a very high value of power factor (near unity).

Fig. 7 demonstrates how the FCSC-rectifier dc output current (i_R) consists of six pulses of the ac line currents. Clearly, there is a duality of operation between the FCSC rectifier (feeding a parallel *RC* load) and a conventional diode bridge rectifier feeding an inductive *RL* load, where the square rectifier input ac currents vary between the positive value of dc load current $+i_d$, zero, and $-i_d$, and where the rectifier output dc voltage is a six-pulse voltage waveform constructed of parts of the ac line voltages. Based on this, the average FCSC-rectifier current can be calculated as follows:

$$I_{\mathrm{dc}} = \frac{1}{\pi/3} \int_{-\pi/6}^{\pi/6} I_m \cos \omega t \ d\omega t \frac{3}{\pi} I_m = 1.35 \ I_{\mathrm{rms}}$$

where I_m and I_{rms} are the maximum and rms values of the input ac current, respectively.

Fig. 8 shows simulated FCSC-rectifier voltage waveforms when operating at the minimum voltage/frequency of 75 V/240 Hz. The voltage across C_c is zero whenever one of the corresponding shunt IGBTs is ON. Figs. 9 and 10 show the corresponding conventional diode bridge rectifier voltage and current waveforms for the same operating conditions. Comparing Fig. 6 with Fig. 9 and Fig. 7 with Fig. 10, the ability of the FCSC rectifier to improve the displacement factor of the ac
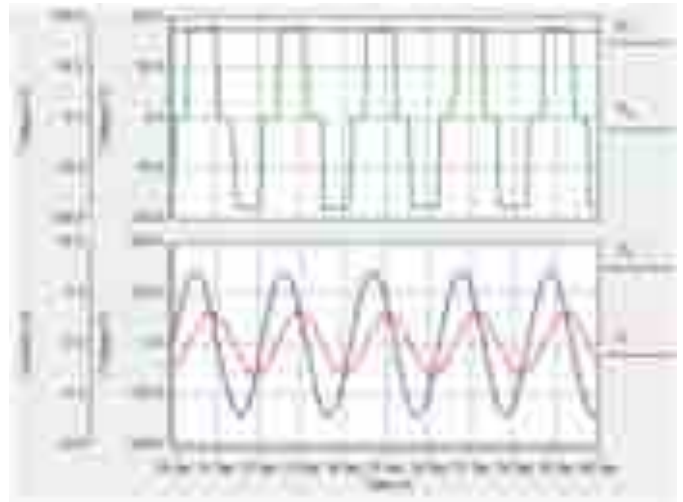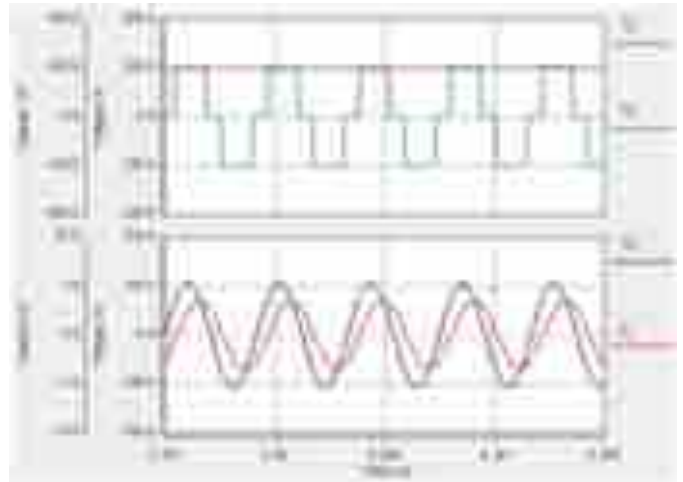
current waveform is highlighted. The phase difference between the ac voltage and current waveforms is almost zero when using the FCSC rectifier, meaning that the FCSC is able to correct the power factor to be almost unity in such a system. Furthermore, there is a dramatic increase in the value of the average output voltage when employing the FCSC rectifier to interface the PM generator. The output voltage is reduced from 191 to 86 V (at 480 Hz) and from 144 to 98 V (at 240 Hz) when using the conventional diode bridge rectifier because of the effects of commutation overlap.

V. EXPERIMENTAL VALIDATION

A 1-kW laboratory test bench was assembled to experimentally verify the behavior of the three-phase FCSC rectifier under various operating conditions. The test bench arrangement is shown in Fig. 11. The PM generator was emulated using a 60 kVA Behlman programmable ac power supply. Three
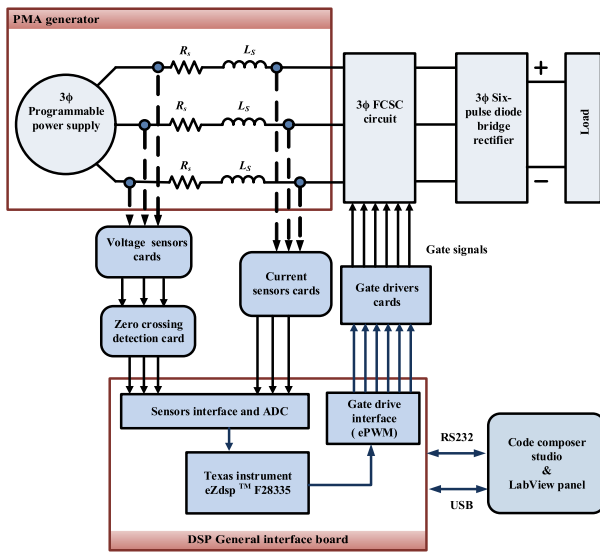
Fig. 11. Experimental test bench arrangement.

Fig. 12. Photograph of the experimental test bench.

TABLE I
LIST OF TEST CIRCUIT COMPONENTS AND THEIR RATINGS

Main components employed in the 1 kW FCSC-rectifier system			
Symbol	Manufacturer	Part number	Typical data
v_s/f_s	Behlman	PAC 2000	60 kVA, rms voltage (0-132 V), frequency (45-500 Hz)
C_C	General electric	97F8248 (Polypropylene film)	8 μF, 660 V AC
S_1-S_6	IXYS	IXDR 30N120	1200 V, 50 A
D_1-D_6	IXYS	VU062-16NO7	1600 V, 63 A
C_L	Panasonic	EETEE2W251LJ (Electrolytic type)	250 μF, 450 V

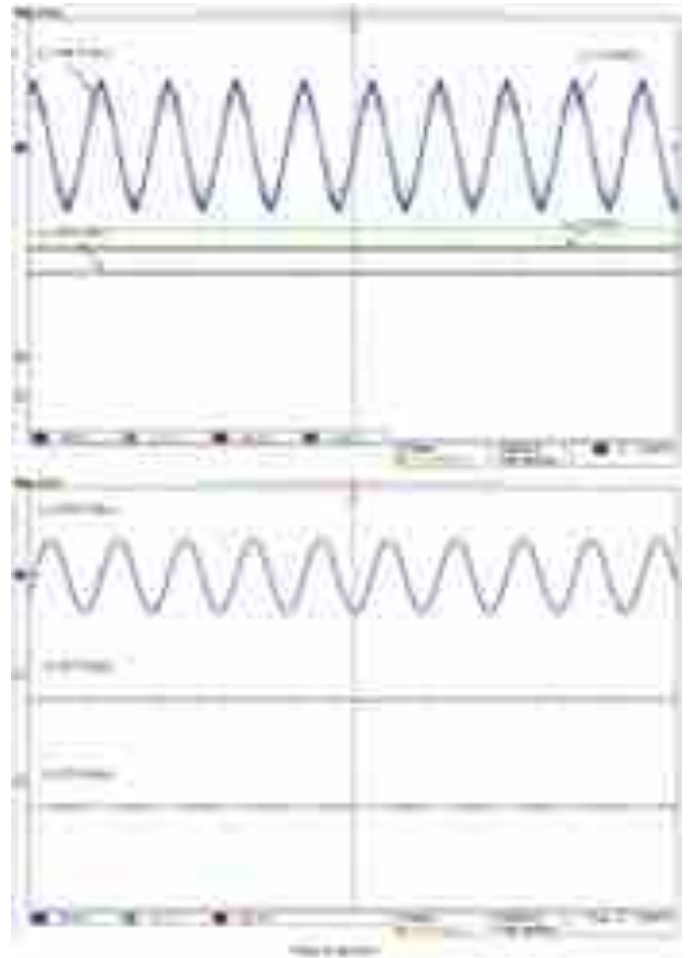Fig. 13. Experimental FCSC-rectifier waveforms at 480 Hz/100 V. v_s: supply phase voltage, i_s: input current, v_L: dc load voltage, i_L: dc load current, and v_{CC}: the voltage across the series capacitor.

dual-gate driver circuits were used to drive the FCSC-rectifier IGBT switches (IXDR 30N120 discrete IGBT modules). An antiparallel diode was not needed because the FCSC rectifier is controlled to maintain resonance and the stored energy in the generator inductance is transferred to the series capacitor without any extreme voltage peaks. Voltage and current sensors were used to detect the input voltages and currents and a zero crossing detector was used to synchronize the firing pulse and determine the IGBT switch ON instances. A controller based on a TMS320F28335 Texas Instruments digital signal processor (DSP) was used to process the sensor's and zero crossing detector (ZCD) card's readings. A host computer was used to monitor and control the system using National Instruments LabView. A photograph of the test bench is shown in Fig. 12. A list of all test circuit components and their ratings is given in Table I.

Figs. 13 and 14 show the experimental waveforms for operation at 100 V/480 Hz and 75 V/240 Hz, respectively. The figure shows that the input current is almost sinusoidal and in-phase

with the generator voltage v_s confirming the effectiveness of the FCSC-rectifier circuit. IGBT timing pulses and the resulting series capacitor voltage are also shown. v_{cc} is zero when S_1 or S_2 is closed in each half-cycle of the generator voltage waveform. The dc load voltage v_L is constant because of the presence of the load capacitor C_L. The corresponding experimental waveforms for the conventional diode bridge rectifier operation are shown in Figs. 15 and 16. The phase shift between the ac current and
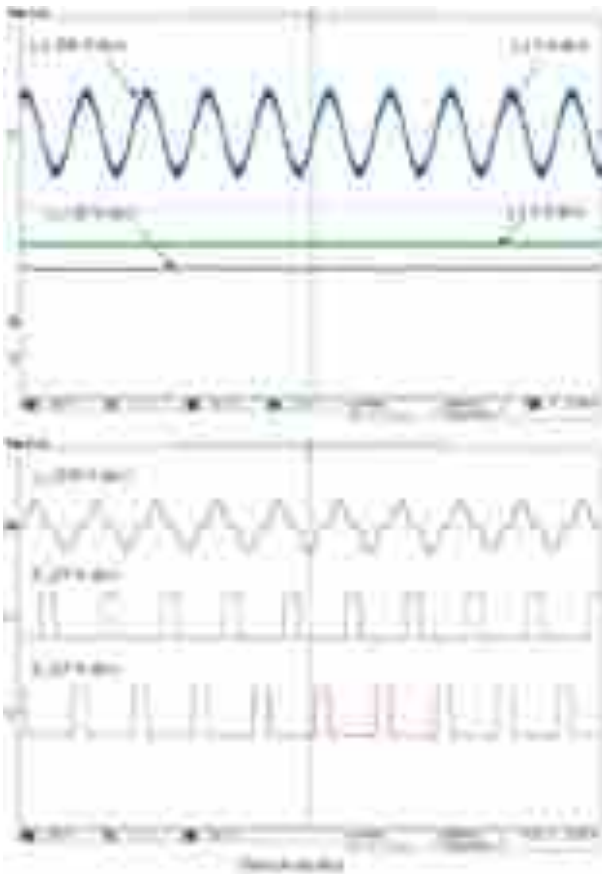
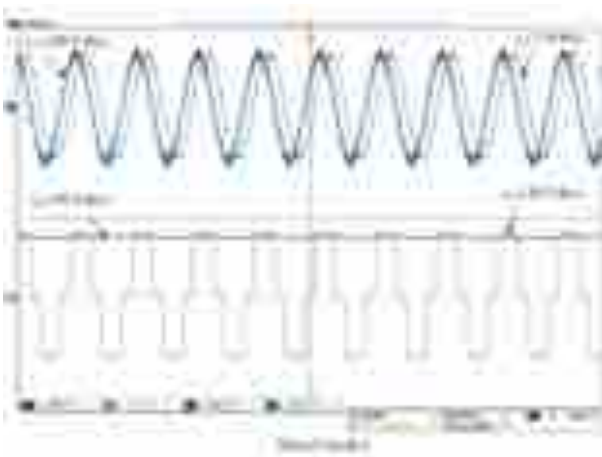Fig. 14.   Experimental FCSC-rectifier waveforms at 240 Hz/75 V.

Fig. 15.   Experimental diode bridge rectifier waveforms at 480 Hz/100 V.

voltage waveforms is evident, as is the reduction in rectifier dc output voltage.

Compared with the conventional diode bridge circuit, the use of the FCSC rectifier enhances the output voltage, output power, and power factor of the system. Table II shows a comparison of the output/input characteristics of both topologies at different load conditions for operation at the nominal aircraft frequency of 400 Hz. When supplying a constant load resistor ($R_L = 30\,\Omega$),

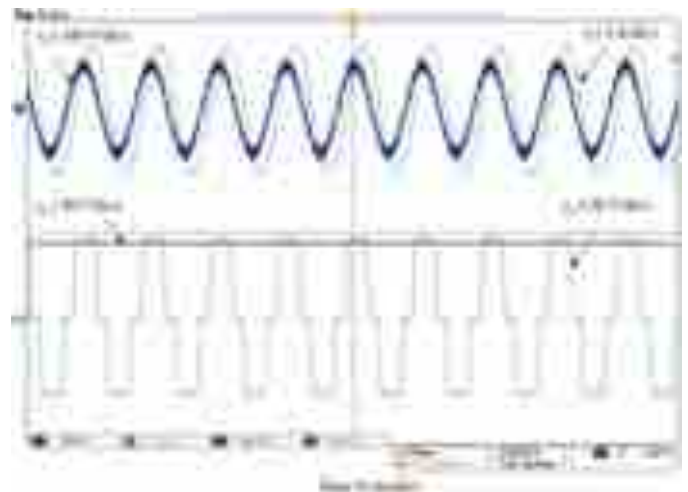
Fig. 16.   Experimental diode bridge rectifier waveforms at 240 Hz/75 V.

TABLE II
COMPARISON OF RECTIFIER CHARACTERISTICS AT 400 HZ ($V_{in} = 90$ V)

R_L (Ω)	Output voltage (V)		Output power (W)		Power factor (lagging)	
	Diode rectifier	FCSC rectifier	Diode rectifier	FCSC rectifier	Diode rectifier	FCSC rectifier
30	82.2	134.9	221.0	667.6	0.57	0.99
25	71.24	128.8	199.5	715.5	0.52	0.99
20	59.8	117.39	173.4	742.4	0.49	0.99
15	45.87	103.05	137.6	761.4	0.42	0.97
10	33	83.27	100.3	780.0	0.35	0.97

TABLE III
COMPARISON OF RECTIFIER CHARACTERISTICS AT DIFFERENT
VOLTAGE/FREQUENCY OPERATING POINTS ($R_L = 30\,\Omega$)

V/f (V/Hz)	Output voltage (V)		Output power (W)		Power factor (lagging)	
	Diode rectifier	FCSC rectifier	Diode rectifier	FCSC rectifier	Diode rectifier	FCSC rectifier
100/480	80	147.7	209.6	817.2	0.51	0.99
90/400	82	134.9	221.9	677.57	0.57	0.99
75/240	91	119	272.09	490.28	0.71	0.95

the FCSC rectifier enhances the output voltage by 64%, output power by 202% and corrects the power factor from 0.57 lagging to almost unity. Even bigger improvements are achieved at higher power outputs (lower values of load resistance). Table III shows the same comparison carried out for operation at three different voltage/frequency operating points with a $30\,\Omega$ constant load resistance. Bigger improvements are obtained at higher voltages and frequencies because of the adverse effects of commutation overlap on the performance of the conventional diode bridge rectifier.

It must be noted, however, that to supply the on-board dc load with power in an MEA at the correct voltage, a dc–dc converter will be needed between the diode bridge rectifier and the dc load to regulate the output voltage level. This part of circuit operation is not considered in this paper that focuses on the rectification
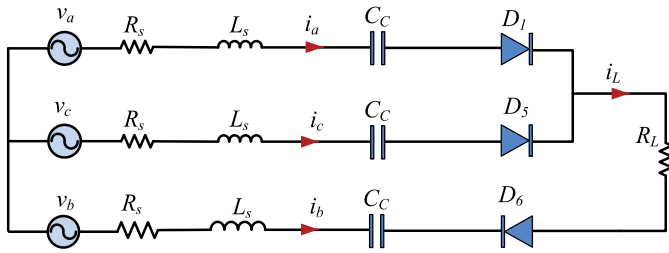
Fig. 17.   Effective circuit during Mode 1-POA with a resistive load.

Fig. 18.   Effective circuit during Mode 1-POA with an inductive load.

process and the steady-state performance of the FCSC-rectifier circuit.

VI. Conclusion

In this paper, an analysis of the performance characteristics of the FCSC rectifier was proposed as a replacement to the conventional diode bridge rectifier that interfaces a stand-alone variable voltage, variable frequency PM generator, and on-board dc loads in MEA. Analysis results were verified experimentally using a 1-kW test rig. The use of the FCSC rectifier is limited to circuits with high series inductance generators/sources and is not an alternative to active PFC converters for a grid operation.

FCSC-rectifier ac input current and dc output voltage waveforms were shown to be the dual of conventional diode bridge rectifier waveforms, with a fundamentally different current commutation process producing a six-pulse dc current waveform. The series compensation FCSC-rectifier circuit produced near sinusoidal ac current waveform in-phase with the generator voltage over a wide range of operational voltages and frequencies achieving operating power factor values of almost unity. Compared with conventional diode rectifier operation, the FCSC rectifier also provided substantial improvements in dc output voltage and output power because it overcame the problems associated with the commutation overlap process in conventional circuits.

Appendix

Circuit Equations: Mode 1, POA; $0 < \omega t < \pi/6 - \delta/2$: D_1, D_5, and D_6 conduct

During this mode of operation, $i_L = i_a + i_c = -i_b$.

1) *Resistive load (R_L):* Fig. 17 shows the effective circuit topology during this subperiod, with the FCSC rectifier supplying current to a resistive load (R_L).

Applying Kirchhoff's voltage law, the circuit can be described by the following equations:

$$L_s \frac{d^2 i_a}{dt^2} - L_s \frac{d^2 i_c}{dt^2} + R_s \frac{di_a}{dt} - R_s \frac{di_c}{dt} + \frac{i_a}{C_c} - \frac{i_c}{C_c} = \frac{dv_{ac}}{dt}$$

$$2L_s \frac{d^2 i_a}{dt^2} + L_s \frac{d^2 i_c}{dt^2} + (2R_s + R_L) \frac{di_a}{dt}$$
$$+ (R_s + R_L) \frac{di_c}{dt} + \frac{2 \, i_a}{C_c} + \frac{i_c}{C_c} = \frac{dv_{ab}}{dt}.$$

Or, in a matrix form

$$\begin{bmatrix} L_s & -L_s \\ 2L_s & L_s \end{bmatrix} \begin{bmatrix} \ddot{i_a} \\ \ddot{i_c} \end{bmatrix} + \begin{bmatrix} R_s & -R_s \\ (2R_s + R_L) & (R_s + R_L) \end{bmatrix} \begin{bmatrix} \ddot{i_a} \\ \ddot{i_c} \end{bmatrix}$$
$$+ \begin{bmatrix} (1/C_c) & -(1/C_c) \\ (2/C_c) & (1/C_c) \end{bmatrix} \begin{bmatrix} i_a \\ i_c \end{bmatrix} = \begin{bmatrix} \dot{v}_{ac} \\ \dot{v}_{ab} \end{bmatrix}. \qquad (3)$$

2) *Series inductive load (RL):* Fig. 18 shows the effective circuit configuration for this sub-period when feeding a series inductive load *(RL)*.

Applying Kirchhoff's voltage law

$$L_s \frac{d^2 i_a}{dt^2} - L_s \frac{d^2 i_c}{dt^2} + R_s \frac{di_a}{dt} - R_s \frac{di_c}{dt} + \frac{i_a}{C_c} - \frac{i_c}{C_c} = \frac{dv_{ac}}{dt}$$

$$(2L_s + L_L) \frac{d^2 i_a}{dt^2} + (L_s + L_L) \frac{d^2 i_c}{dt^2} + (2R_s + R_L) \frac{di_a}{dt}$$
$$+ (R_s + R_L) \frac{di_c}{dt} + \frac{2 \, i_a}{C_c} + \frac{i_c}{C_c} = \frac{dv_{ab}}{dt}.$$

Or, in a matrix form

$$\begin{bmatrix} L_s & -L_s \\ (2L_s + L_L) & (L_s + L_L) \end{bmatrix} \begin{bmatrix} \dot{i_a} \\ \dot{i_c} \end{bmatrix}$$
$$+ \begin{bmatrix} R_s & -R_s \\ (2R_s + R_L) & (R_s + R_L) \end{bmatrix} \begin{bmatrix} i_a \\ i_c \end{bmatrix}$$
$$+ \begin{bmatrix} (1/C_c) & -(1/C_c) \\ (2/C_c) & (1/C_c) \end{bmatrix} \begin{bmatrix} i_a \\ i_c \end{bmatrix} = \begin{bmatrix} \dot{v}_{ac} \\ \dot{v}_{ab} \end{bmatrix} \qquad (4)$$

where L_L is the load inductance.

Circuit Equations: Mode 1, POB; $\pi/6 - \delta/2 < \omega t < \pi/6 + \delta/2$: S_4 ON, D_1, D_5, and D_6 Conduct

During this mode of operation, $i_L = i_a + i_c = -i_b$.

1) *Resistive load:* The effective circuit topology during this subperiod is shown in Fig. 19.

Applying Kirchhoff's voltage law

$$L_s \frac{d^2 i_a}{dt^2} - L_s \frac{d^2 i_c}{dt^2} + R_s \frac{di_a}{dt} - R_s \frac{di_c}{dt} + \frac{i_a}{C_c} - \frac{i_c}{C_c} = \frac{dv_{ac}}{dt}$$

$$2L_s \frac{d^2 i_a}{dt^2} + L_s \frac{d^2 i_c}{dt^2} + (2R_s + R_L) \frac{di_a}{dt}$$
$$+ (R_s + R_L) \frac{di_c}{dt} + \frac{i_a}{C_c} = \frac{dv_{ab}}{dt}.$$
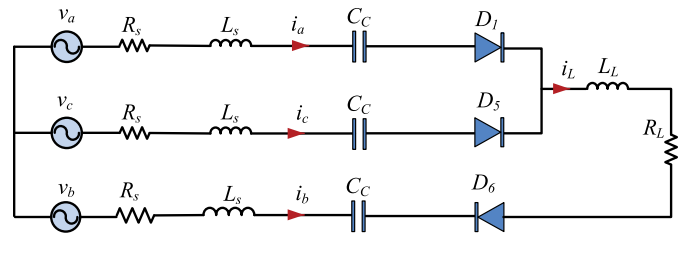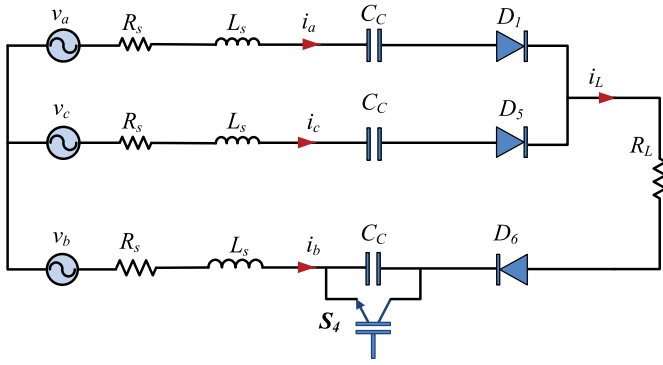
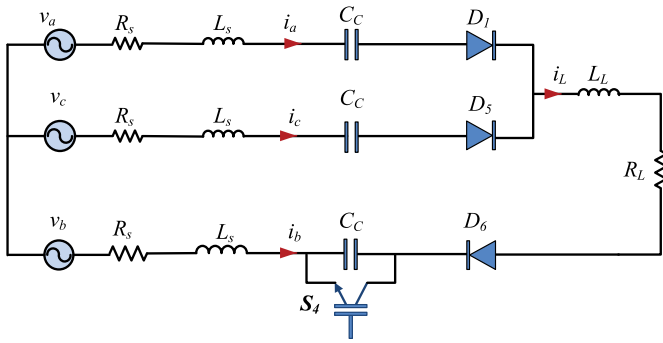Fig. 19. Effective circuit during Mode 1-POB with a resistive load.

Fig. 20. Effective circuit during Mode 1-POB with an inductive load.

Or, in a matrix form

$$
\begin{bmatrix} L_s & -L_s \\ 2L_s & L_s \end{bmatrix} \begin{bmatrix} \ddot{i}_a \\ \ddot{i}_c \end{bmatrix}
$$
$$
+ \begin{bmatrix} R_s & -R_s \\ (2R_s + R_L) & (R_s + R_L) \end{bmatrix} \begin{bmatrix} \dot{i}_a \\ \dot{i}_c \end{bmatrix}
$$
$$
+ \begin{bmatrix} (1/C_c) & -(1/C_c) \\ (1/C_c) & 0 \end{bmatrix} \begin{bmatrix} i_a \\ i_c \end{bmatrix} = \begin{bmatrix} \dot{v}_{ac} \\ \dot{v}_{ab} \end{bmatrix}. \qquad (5)
$$

2) *RL load:* Fig. 20 shows the effective circuit configuration with a series *RL* load.

Applying Kirchhoff's voltage law

$$
L_s \frac{d^2 i_a}{dt^2} - L_s \frac{d^2 i_c}{dt^2} + R_s \frac{di_a}{dt} - R_s \frac{di_c}{dt} + \frac{i_a}{C_c} - \frac{i_c}{C_c} = \frac{dv_{ac}}{dt}
$$
$$
(2L_s + L_L) \frac{d^2 i_a}{dt^2} + (L_s + L_L) \frac{d^2 i_c}{dt^2} + (2R_s + R_L) \frac{di_a}{dt}
$$
$$
+ (R_s + R_L) \frac{di_c}{dt} + \frac{i_a}{C_c} = \frac{dv_{ab}}{dt}.
$$

Or, in a matrix form

$$
\begin{bmatrix} L_s & -L_s \\ (2L_s + L_L) & (L_s + L_L) \end{bmatrix} \begin{bmatrix} \ddot{i}_a \\ \ddot{i}_c \end{bmatrix}
$$

$$
+ \begin{bmatrix} R_s & -R_s \\ (2R_s + R_L) & (R_s + R_L) \end{bmatrix} \begin{bmatrix} \dot{i}_a \\ \dot{i}_c \end{bmatrix}
$$
$$
+ \begin{bmatrix} (1/C_c) & -(1/C_c) \\ (1/C_c) & 0 \end{bmatrix} \begin{bmatrix} i_a \\ i_c \end{bmatrix} = \begin{bmatrix} \dot{v}_{ac} \\ \dot{v}_{ab} \end{bmatrix}. \qquad (6)
$$

REFERENCES

[1] P. Wheeler and S. Bozhko, "The more electric aircraft: Technology and challenges," *IEEE Electrific. Mag.*, vol. 2, no. 4, pp. 6–12, Dec. 2014.

[2] Y. Huangfu, S. Pang, B. Nahid-Mobarakeh, L. Guo, A. K. Rathore, and F. Gao, "Stability analysis and active stabilization of on-board DC power converter system with input filter," *IEEE Trans. Ind. Electron.*, vol. 65, no. 1, pp. 790–799, Jan. 2018.

[3] A. Malik and A. khaligh, "Intermediate DC-link capacitor reduction in a two-stage cascaded AC–DC converter for more electric aircrafts," *IEEE Trans. Veh. Technol.*, vol. 67, no. 2, pp. 935–947, Feb. 2018.

[4] L. Tarisciotti, A. Costabeber, C. Linglin, A. Walker, and M. Galea, "Evaluation of isolated DC–DC converter topology for future HVDC aerospace microgrid," in *Proc. IEEE Energy Convers. Congr. Expo.*, Cincinnnati, OH, USA, 2017, pp. 2238–2245.

[5] P. Wheeler, "Technology for the more and all electric aircraft of the future," in *Proc. IEEE Int. Conf. Autom.*, Curico, Chile, 2016, pp. 1–5.

[6] H. Abu-Rub, M. Malinowski, and K. Al-Haddad, *Power Electronics for Renewable Energy Systems, Transportation and Industrial Applications*. Chichester, U.K.: Wiley-IEEE Press, 2014.

[7] G. Buticchi, L. Costa, and M. Liserre, " Improving system efficiency for the more electric aircraft: A look at dc–dc converters for the avionic onboard dc microgrid," *IEEE Ind. Electron. Mag.*, vol. 11, no. 3, pp. 26–36, Sep. 2017.

[8] B. Sarlioglu and C. T. Morris, "More electric aircraft: Review, challenges, and opportunities for commercial transport aircraft," *IEEE Trans. Transport. Electrific.*, vol. 1, no. 1, pp. 54–64, Jun. 2015.

[9] Z. Zhang, J. Huang, Y. J. W. Geng, and Y. Xu, "Overview and analysis of PM starter/generator for aircraft electrical power systems," *CES Trans. Elect. Mach. Syst.*, vol. 1, no. 2, pp. 117–131, Jul. 2017.

[10] J. Chen, C. Wang and J. Chen, "Investigation on the selection of a more suitable power system architecture for future more electric aircraft from the prospective of system stability," in *Proc. IEEE 26th Int. Symp. Ind. Electron.*, Edinburgh, U.K., 2017, pp. 1861–1867.

[11] A. Mallik and A. Khaligh, "Comparative study of three-phase buck, boost and buck-boost rectifier topologies for regulated transformer rectifier units," in *Proc. IEEE Transport. Electrific. Conf. Expo*, Dearborn, MI, USA, 2015, pp. 1–7.

[12] J. Benzaquen, M. B. Shadmand, A. Stonestreet, and B. Mirafzal, "A unity power factor active rectifier with optimum space-vector predictive DC voltage control for variable frequency supply suitable for more electric aircraft applications," in *Proc. IEEE Appl. Power Electron. Conf. Expo.*, San Antonio, TX, USA, 2018, pp. 1455–1460.

[13] A. Mallik, W. Ding, and A. Khaligh, "A comprehensive design approach to an EMI filter for a 6-kW three-phase boost power factor correction rectifier in avionics vehicular systems," *IEEE Trans. Veh. Technol.*, vol. 66, no. 4, pp. 2942–2051, Apr. 2017.

[14] G. Sivanagaraju, A. K. Rathore, and D. M. Fulwani, "Discontinuous conduction mode three phase buck-boost derived PFC converter for more electric aircraft with reduced switching, sensing and control requirements," in *Proc. IEEE Appl. Power Electron. Conf. Expo.*, San Antonio, TX, USA, 2018, pp. 1467–1472.

[15] J. Kolar and T. Friedli, "The essence of three-phase PFC rectifier systems—Part I," *IEEE Trans. Power Electron.* vol. 28, no. 1, pp. 176–198, Jan. 2013.

[16] A. Singh, A. Mallik, and A. Khaligh, "A comprehensive design and optimization of the DM EMI filter in a boost PFC converter," *IEEE Trans. Ind. Appl.*, vol. 54, no. 3, pp. 2023–2031, May/Jun. 2018.

[17] "Environmental conditions and test procedures for airborne equipment," RTCA, Inc., Washington, DC, USA, RTCA Document no. RTCA DO-160E, Dec. 2010.

[18] T. Al-Mhana, V. Pickert, D. Atkinson, and B. Zahawi, "Forced commutated controlled series capacitor rectifier for more electric aircraft," *IEEE Trans. Power Electron.*, vol. 34, no. 1, pp. 225–235, Jan. 2019.

Tahani H. M. Al-Mhana (M'18) received the B.Sc. degree in electrical engineering from Mosul University, Mosul, Iraq, in 1992, the M.Sc. degree in electrical engineering from the University of Technology, Baghdad, Iraq, in 2000, and the Ph.D. degree in electrical and electronic engineering from Newcastle University, Newcastle upon Tyne, U.K., in 2016.

Since 1992, she has been with the Department of Electrical Engineering, University of Babylon, Hilla, Iraq, where she is currently a Lecturer in Electrical Machines and Power Electronics. Her research interests include power electronics and its applications such as in more electric aircraft, wave energy converter, harmonics, electrical machines control, series compensations, and power factor corrections.

Bashar Zahawi (M'96–SM'04) received the B.Sc. and Ph.D. degrees in electrical and electronic engineering from Newcastle University, Newcastle upon Tyne, U.K., in 1983 and 1988, respectively.

From 1988 to 1993, he was a Design Engineer with a U.K. manufacturer of large variable speed drives and other power conversion equipment. He was appointed as a Lecturer in electrical engineering with the University of Manchester, Manchester, U.K., in 1994, and was a Senior Lecturer with the School of Electrical and Electronic Engineering, Newcastle University, from 2003 to 2014. Since 2014, he has been with the Department of Electrical and Computer Engineering, Khalifa University, Abu Dhabi, United Arab Emirates, where he is currently a Professor in Electrical Power Engineering.

Dr. Zahawi was the recipient of the Crompton Premium, awarded by the Institution of Electrical Engineers, U.K., and the Denny Medal, awarded by the Institute of Marine Engineering, Science & Technology, U.K.

Volker Pickert (M'04) received the Dipl.-Ing. degree in electrical and electronic engineering from the Rheinisch-Westfaelische Technische Hochschule (RWTH), Aachen, Germany, in 1994, and the Ph.D. degree in power electronics from Newcastle University, Newcastle upon Tyne, U.K., in 1997. He also studied electrical and electronic engineering at Cambridge University, Cambridge, U.K.

He was with Semikron GmbH, Germany, as a Product Manager and later with Volkswagen AG., Germany, as an research and development (R&D) Group Head for electric vehicles power drive train development. In 2003, he was appointed as a Senior Lecturer with Newcastle University, where he became a Full Professor in 2011 and the Head of the Electrical Power Group in 2012. His current research interests include power electronics for automotive applications, thermal management, health monitoring techniques, and advanced nonlinear control.

Dr. Pickert is the Editor-in-Chief of the *IET Power Electronics* journal. He was the Conference Chairman of the biannual international institution of engineering and technology (IET) power electronics, machines and drives (PEMD) conference 2010 in Brighton, U.K., and is a regular invited keynote speaker. He was the recipient of the Denny Medal from institute of marine engineering, science and technology (IMarEST) for the best journal paper in 2011 in marine applications and the Best Paper Award at the IEEE International Conference on Computing, Electronics & Communications Engineering (iCCECE 2018).

David J. Atkinson received the B.Sc. degree in electrical and electronic engineering from Sunderland Polytechnic, Sunderland, U.K., in 1978, and the Ph.D. degree in electrical and electronic engineering from Newcastle University, Newcastle upon Tyne, U.K., in 1991.

He is a Senior Lecturer with the Drives, Electrical Power Group, School of Engineering, Newcastle University, Newcastle upon Tyne. His research interests include electrical drive systems and power electronics control for new and renewable energy systems. Prior to his university appointment in 1987, he had spent 17 years in the electronics industry including periods with NEI Electronics, Hebburn, U.K., and British Gas Corporation, Cramlington, U.K.

Dr. Atkinson was the recipient of the IEE Power Premium Prize.